Cellular and Molecular Bioengineering, Vol. 1, Nos. 2–3, September 2008 *(© 2008)* pp. 110–121
DOI: 10.1007/s12195-008-0027-5

A Multi-Scale Mechanistic Model for Actin-Propelled Bacteria

RICHARD B. DICKINSON[1,2]

[1]Department of Chemical Engineering, University of Florida, Gainesville, FL 32611-6005, USA; and [2]Department of Biomedical Engineering, University of Florida, Gainesville, FL 32611-6005, USA

(Received 29 August 2008; accepted 24 September 2008; published online 23 October 2008)

Abstract—Some invasive bacterial pathogens propel themselves intracellularly by hijacking the host cell's actin assembly machinery to polymerize actin filaments into a dense "comet tail" network of filamentous actin. The bacterium is propelled forward as new actin monomers incorporate into filament ends positioned at the bacterial surface. How the bacterium remains firmly attached to the elongating end of the actin tail during propulsion remains a central question in actin-based motility. Here, a mechanistic model, based on the filament end-tracking motor ("actoclampin") hypothesis, is proposed to explain some emergent features of actin-based propulsion, including the alignment of filaments with the direction of motion, rotation about the axis of motion, and helical trajectories. Simulation of the model shows that these features should arise naturally from diffusion-limited elongation of an ensemble of filaments that are strongly anchored at their elongating ends to the bacterial surface by end-tracking proteins. These results suggest that a persistent torsion and curvature of the actin comet tail does not require a filament torque (created by insertional elongation of helical filaments), although a small right-handed filament torque is sufficient to ensure symmetry breaking toward a right-handed torsion.

Keywords—Listeria, Actin-based motility, Nucleation promoting factor, Rickettsia, Shigella, ActA, IcsA, RickA, Actoclampin, Filament end-tracking motor.

INTRODUCTION

Actin polymerization generates the forces necessary for propulsion of intracellular pathogens such as *Listeria*, *Shigella*, *Burkholderia*, and *Rickettsia*.[42] How the energy released by polymerization is captured to generate propulsive forces remains an open question. Even beyond its immediate significance to understanding pathogenesis of infections by these microbes, elucidating the biochemical and biophysical basis for propulsive force generation by actin polymerization has wide relevance in cell biology, because the underlying force generation mechanism is likely similar to those involved in membrane protrusion during cell crawling and numerous other cell functions driven by actin-based force generation.

Actin-based motility of bacteria and other particles requires the particles to be coated with filament nucleation promoting factors (NPFs), which bind actin monomers and activate the filament nucleator Arp2/3 complex.[9,10,45] For *Listeria*, the surface protein ActA serves this function, and ActA's ability to support motility is greatly enhanced when it recruits the host-cell NPF, Vasodilator-stimulated Phosphoprotein (VASP), a member of the Ena/VASP and WASP (Wiskott Aldrich Syndrome Protein) family of NPF proteins.[8,9] Similarly, the microbial surface protein RickA[17] from Rickettsia and BimA[43] are bacterial analogues to Neuronal-WASP (N-WASP), whereas the Shigella surface protein IcsA captures the N-WASP from the host cell cytoplasm.[18,44]

Filaments nucleated from NPF's form a dense F-actin network to ultimately form an F-actin rich "comet" tail (Fig. 1), into which new actin monomers incorporate by adding to filament tips located at the bacterial surface. When the comet tail is anchored to the cytoskeleton, the microbe moves relative to the fixed reference frame as the tail elongates. Trajectories of propelled bacteria have exhibited a number of interesting properties, including persistent longitudinal rotation[36] about the axis of motion, as well as persistent helical trajectories.[47] One goal of the model presented here is to explain these types of motions in terms of the filament growth mechanism.

Micrographs of comet tails from several studies show the filament microstructure of tails can vary considerably depending on the type of bacteria and medium conditions. As depicted in Fig. 1, many filaments in the tail appear aligned in the direction of propulsion with their plus ends located at the surface, while other filaments (typically shorter) may be directed outward from the tail,[5] sometimes giving a "fishbone" appearance. Brieher *et al.*[5] reported that when

Address correspondence to Richard B. Dickinson, Department of Chemical Engineering, University of Florida, Gainesville, FL 32611-6005, USA. Electronic mail: dickinso@che.ufl.edu

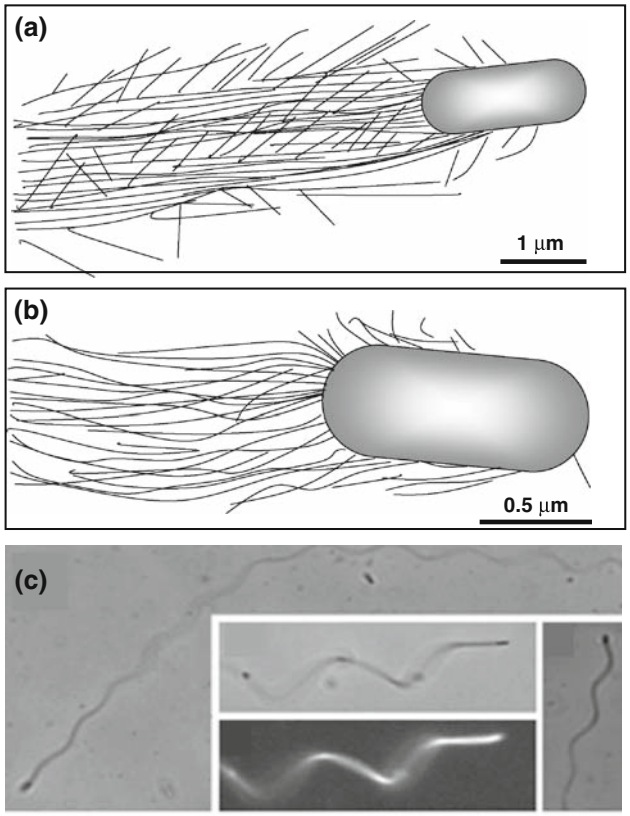

FIGURE 1. Structure of actin comet tails behind microbial pathogens. (a) Depiction of *Listeria monocytogenes* tail consisting of parallel filaments terminating at the microbial surface and as well as many branches terminating away from the surface (after Fig. 2c in Brieher *et al.*[5]). (b) Depiction of *Rickettsia conorii* with parallel filaments terminating at the surface with no Arp2/3 branches (after Fig. 5 in Gouin *et al.*[18]). (c) Phase contrast and fluorescence micrographs of *Listeria* tails exhibiting persistent helices (image is from Zeile *et al.*[47]).

Arp2/3 is inhibited this latter class of filaments disappears and propulsion speed is actually enhanced, suggesting that these filaments are Arp2/3-nucleated branches emanating at the characteristic 70° angles from the parallel filaments and are not responsible for force generation. Indeed, some micrographs of propelled bacteria show essentially no branches (as depicted in Fig. 1b), with nearly all filaments oriented in the propulsion direction and (+)-ends appearing to terminate at the bacterial surface. For these reasons, Arp2/3-mediated filament branches are assumed to be unessential to the propulsion mechanism and are thus ignored in the treatment of the model presented here.

The actin rocket tail is firmly attached to bacterial surface NPF's by a mechanism that is a currently unknown but subject to various theories. One proposal is that attachment results from transient binding between the NPF on the bacterial surface and Arp2/3 bound to the side of an existing filament during the nucleation of a filament branch.[39] However, efficient propulsion[5] and tail attachment[10] under Arp2/3 inhibition, as well as the lack of branches in some microbial tails (Fig. 1b), argue against direct Arp2/3-NPF binding as the dominant tail-attachment mechanism in microbial propulsion. Other proposals are that surface-associated NPF's continue to associate with the filaments (+)-ends following nucleation, either by binding and unbinding between monomer addition from solution,[10] or, persistently by a processive insertional polymerization mechanism,[11,12] similar to the confirmed action of formin NPF's.[11] The model presented here explores the consequences of the latter hypothesis and shows that a number of experimentally observed motility properties emerge naturally from the filament end-tracking mechanism.

This paper presents a three-dimensional model and multi-scale simulation for bacterial propulsion by actin-based motility. The general goal of this model is to predict microbial trajectories on the long time scale (minutes) and large length scale (many microns), in terms of molecular processes involved in filament elongation (diffusion/and monomer binding) and the flexural mechanics of individual actin filaments located at the microbe surface. In addition to the issue of tail attachment, other questions addressed by the model presented here include: How does parallel alignment of working filaments in the actin network emerge? What is the explanation for persistent longitudinal rotation and helical trajectories? Simulations based on the model show that these emergent properties of bacterial trajectories should arise naturally from diffusion-limited elongation of filaments attached to the surface via filament end-tracking motors.

MODEL FORMULATION

The trajectory of a microbe undergoing actin-based motility is determined from the balance of forces and moments generated by the ensemble of elongating filaments interacting with the bacterial surface. Individual filaments elongate at a rate that depends on filament load and on the local monomer concentration. A simulation of the propulsion trajectory therefore requires a model for force-dependent filament elongation, while accounting local variations in monomer concentration arising from diffusion limitations. The forces and torques generated by individual filaments depend on their orientations and positions on the microbial surface as well as how the filament stresses are transmitted into the highly cross-linked actin tail.

A. Morphology and Kinematics

To facilitate comparison to *Listeria* trajectories, the analysis is confined to a pill-shaped particle of radius R

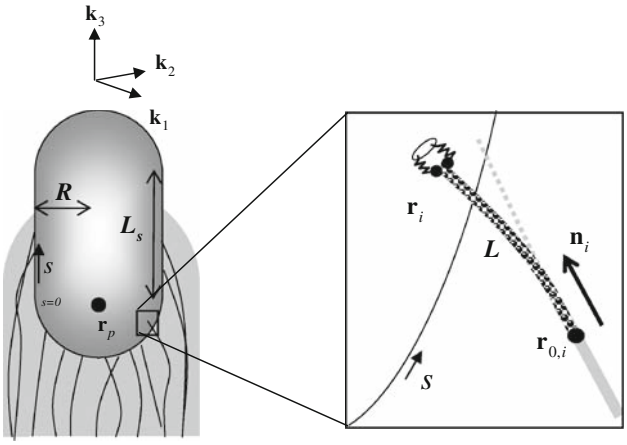

FIGURE 2. Schematic showing the model variables and parameters. The model bacterium of radius *R* and side length L_s, is coated with a nucleation promoting factors (NPF) at a mean density concentrated to one pole. An individual filaments is assumed bound at the (+)-end to an NPF located at r_i and anchored at position $r_{0,i}$ located at filament free-segment length *L* from the tip. The NPF has a spring constant, and the filament mechanics are determined by its bending stiffness. The position vector r_p identifies the center of the rearward half-sphere, and the instantaneous orientation is identified by directors (orthogonal unit vectors) k_1, k_2, and k_3. The NPF density depends on the contour position *s*, where *s* = 0 is taken as the boundary position between spherical and cylindrical regions of the pill-shaped bacterium.

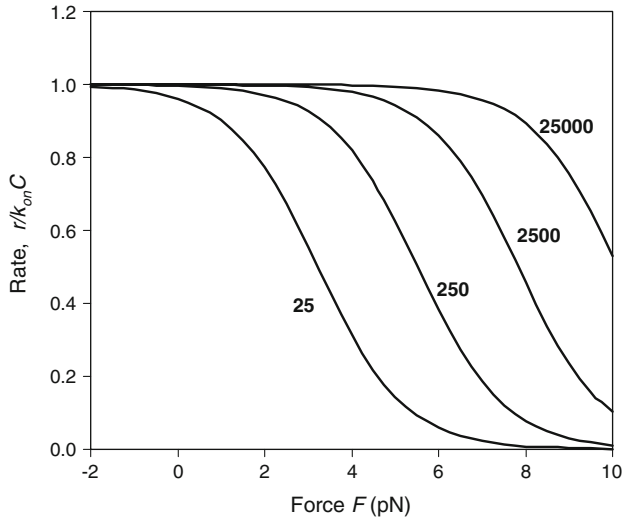

FIGURE 3. Force-dependent elongation rate based on the filament end-tracking motor model. Elongation rate (scaled to $k_f C$, where k_f is the monomer-binding rate constant and *C* is the local monomer concentration) is plotted against force assuming filament end-tracking motor kinetics (Eq. 3), for different values of the ratio $k_{f0}/k_f C$, where k_{f0} is monomer incorporation rate for an unstressed filament. Note the predicted insensitivity of elongation rate to moderate forces for fast monomer incorporation (i.e., large values of $k_{f0}/k_f C$). The parameter values used in the simulations correspond to $k_{f0}/k_f C$ = 250.

and side-length L_s (assumed equal to $2R$) (Fig. 2). Let $\mathbf{r}_p(t)$ identify the instantaneous position (identified by the center of the rear half-sphere) and the directors $\mathbf{k}_1(t)$, $\mathbf{k}_2(t)$, $\mathbf{k}_3(t)$ (orthogonal unit vectors) identify the orientation. The net force and moments are assumed to be in balance with drag forces, such that

$$\beta \frac{d\mathbf{r}_p}{dt} = \mathbf{F} \tag{1}$$

$$\beta_r \frac{d\mathbf{k}_i}{dt} = \mathbf{T} \times \mathbf{k}_i \quad i = 1, 2, 3 \tag{2}$$

where β and β_r are the translational and rotational drag coefficients, respectively. As discussed below, the applied forces include those generated by individual filament (+)-ends (discussed below), as well as a steric force that prevents the microbial boundary from crossing the actin network.

B. Filament Growth Model

Individual elongating filament ends are assumed to be anchored to the microbial surface via NPF's acting as filament end-tracking proteins, which bind and facilitate the processive elongation of the filament (+)-end.[11] According to the theory of end-tracking motors, the net cycle of monomer addition involves a force-insensitive monomer-binding step (rate $k_{on}C$) followed by a force (F)-sensitive transition step (with rate constant $k_t(F)$) in which the monomer is incorporated into the filament tip. Assuming each step is irreversible, a rate expression for monomer addition consistent with these properties is

$$r(F) = \frac{k_{on}C}{1 + \frac{k_{on}C}{k_t(F)}}, \tag{3}$$

Eq. (3) has the property that for smaller forces, when $k_t(F) >> k_{on}C$, elongation is insensitive to force and thus rate-limited by the monomer binding rate. As long as this property is preserved for forces up to 5–10 pN, the model predictions are insensitive to the precise form of Eq. (3). A reasonable expression for the force-dependent monomer-incorporation rate that captures this behavior is $k_t(F) = k_{t,0}e^{-Fd/k_BT}$, which presumes a transition state barrier positioned at a distance d = 2.7 nm, which is the added filament length upon the addition of one monomer. Equation (3) is plotted in Fig. 3 for various values of $k_{t,0}$.

Before the simulations, NPF's were initially placed randomly on the bacterial surface with probability that corresponded to specified mean surface density ρ ($\#/\mu m^2$). (Here and hereafter an "NPF" refers to a functional filament nucleating and end-tracking unit at a surface density that corresponds to the local

TABLE 1. List of parameters.

Symbol	Parameter	Range	Source(s)	Value used	Model sensitivity[a]
a	Monomer capture radius			3.5 nm	–
β	Drag coefficient		Calculated	0.07 pN s/μm	–
β_r	Rotational drag coefficient		Calculated	0.05 pN μm s	–
C_∞	Bulk monomer concentration	1–20 μM	30,34	4 μM	–
d	Added filament length per monomer		19	2.7 nm	
D	Monomer diffusion coefficient	2–15 $\mu m^2/s$	13,27,32,33	5 $\mu m^2/s$	+
ε	Cauchy distribution parameter			Varied	+
F_c	Filament detachment force	>5 pN	46	10 pN	++
k_n	Nucleation rate constant		Estimated	1 s^{-1}	+
$k_{d,0}$	Based detachment rate constant	<0.1 s	23	0.01 s^{-1}	+
κ_m	NPF stiffness	1–10 pN/nm	20	1 pN/nm	–
$\kappa_{f,\|\|}, \kappa_{f,\perp}$	Filament spring constants		Calculated		+
k_{on}	Monomer on-rate constant	10–100 $\mu M^{-1}s^{-1}$	37	10 $\mu M^{-1}s^{-1}$	+
$k_{t,0}$	Monomer transfer rate constant	10^4–10^6 s^{-1}	11	10^4 s^{-1}	+
κ_s	Cell surface stiffness			10 pN/nm	–
λ	Filament persistence length	5–15 μm	22	10 μm	+
L	Uncross-linked filament segment length	50–200 nm	31	100 nm	+
L_d	NPF density decay length	0.1–3 μm	35	0.3 μm	+
L_s	Bacteria side length	0.5–2 μm		0.8 μm	
ρ_0	Maximum NPF/filament tip density	500–1500 μm^{-2}	1,40	10^3 μm^{-2}	+
R	Bacterial radius			0.4 μm	

[a]Indicates sensitivity of motile behavior (e.g., emergence of filament alignment, torsion, etc.) to parameter values.

maximum density of filament ends. The actual surface density of NPF's molecules may exceed this value. For example, the end-tracking mechanism anticipates that at least two NPF molecules are required per filament tip[11]). To reflect the distribution of ActA on *Listeria*,[35] the rearward half-sphere was assumed uniform with density ρ_0, with the density on the sides decreasing exponentially with arc length s (see Fig. 2), i.e., $\rho(s) = \rho_0 e^{-\max(s,0)/L_s}$ with decay constant L_d. During random placement of NPF's (by random number generation), any new NPF placed within one filament diameter (7 nm) of an existing NPF was rejected and another was added elsewhere. In order to explore the possible effects an asymmetric distribution around the long axis, in some simulations NPF's were concentrated in the azimuth θ according to the wrapped Cauchy density,[14]

$$\rho(\theta, s) = \rho_{\max}(s) \frac{(1-\varepsilon)^2}{1+\varepsilon^2-2\varepsilon\cos\theta} \tag{4}$$

where $\rho_{\max}(s) = \rho_0 e^{-\max(s,0)/L_s}$. As is presumably true for the actual pathogen, the polar concentration of NPF's facilitates symmetry breaking and the onset of directional motility in the simulations. Also, because the actin gel outside the zone of filament flexure is treated as rigid, symmetry breaking in the simulations is not possible when the microbe is completely coated with NPF's. A more realistic treatment of actin network mechanics (see "Discussion") would be required for an accurate model of symmetry breaking. However, since our focus is on the emergent trajectories on the long time scale, this limitation is not considered severe.

C. Monomer Concentration Field

In addition to stochastic growth, another important source of a variation in elongation rate (and thus forces) among the filament population is a gradient in monomer concentration C along the microbial surface. Significant concentration gradients are expected to arise when the characteristic reaction speed ($k_{on}\rho$) is similar to (or larger than) the characteristic diffusion speed (D/R) to the microbial surface.[13] Thus, the dimensionless group that characterizes whether elongation is reaction- or diffusion-rate limited is the Damköhler number $D_a \equiv k_{on}\rho R/D$. For bacterial propulsion by actin-based motility, typical values for the parameters (Table 1) are $k_{on} = 10\ \mu M^{-1}s^{-1}$ ($=0.017\ \mu m^3/s$), $\rho = 10^3\ \mu m^{-1}$, $R = 0.5\ \mu$m, and $D = 5\ \mu m^2/s$, D_a is ~2, suggesting the presence of a significant diffusion-rate limitation to filament elongation and formation of monomer concentration gradients. These spatial variations in filament growth rates should generate significant stress gradients on the surface.[13]

The calculation of the monomer concentration field surrounding the microbe requires solution of the diffusion equation with point sinks at the filament tips, accounting for the non-penetrating boundary of the microbial surface. However, because the diffusion time

($R^2/D \sim 50$ ms) is expected to be short relative to the time required for elongation to yield significant displacements ($R/rd > 1$ s), the concentration profile should remain at a quasi-steady state on the relevant time scale and well-approximated by the solution to the Laplace equation ($\nabla^2 C = 0$). (Although filaments grow stochastically, which many result in temporal fluctuations in the monomer field, of interest is the mean monomer concentration field, so it is self-consistent to use the deterministic rates obtained from Eq. (3) in order to calculate $C(\mathbf{r})$.)

From potential theory,[4] the solution to Laplace equation on the domain surrounding the microbe can be expressed as an integral on the surface Γ, i.e.,

$$C(\mathbf{r}) = C_\infty - \left(\int_\Gamma \sigma(\mathbf{r}') u^*(\mathbf{r}, \mathbf{r}') d\Gamma(\mathbf{r}') + \frac{2}{D} \sum_j r_j(C(\mathbf{r}_j)) u^*(\mathbf{r}, \mathbf{r}_j) \right) \tag{5}$$

where $\sigma(\mathbf{r})$ is an unknown continuous surface function, r_j is the consumption rate (#/s—c.f. Eq. 3) at filament end j located at surface position $\mathbf{r}_j$, and $u^*(\mathbf{r}, \mathbf{r}') = \frac{1}{4\pi|\mathbf{r}-\mathbf{r}'|}$ is the fundamental solution of Laplace equation. Monomers reaching an encounter radius a from the filament end are consumed by polymerization, such that the concentration at the tip of filament j is given by

$$C(\mathbf{r}_i) = C_\infty - \left(\int_\Gamma \sigma(\mathbf{r}') u^*(\mathbf{r}_i, \mathbf{r}') d\Gamma(\mathbf{r}') + \frac{1}{2\pi D a} r_i + \frac{2}{D} \sum_{j \neq i} r_j(C(\mathbf{r}_j)) u^*(\mathbf{r}_i, \mathbf{r}_j) \right) \tag{6}$$

For these simulations, the value $a = 3.5$ nm was chosen, corresponding to a filament radius, but it should be noted that the solution is insensitive to the value of a as long as it is much smaller than the filament spacing (i.e., $a << \rho^{-1/2}$). An additional equation relating the concentration at the filament tips to the unknown surface density is obtained by imposing a no-flux boundary condition at the surface, which is achieved by differentiating Eq. (6) with respect to the outward normal direction and equating it to zero:

$$n(\mathbf{r}) \cdot \frac{\partial C(\mathbf{r})}{\partial \mathbf{r}} = 0 = \frac{1}{2}\sigma(\mathbf{r}) - \int_\Gamma \sigma(\mathbf{r}') \frac{n(\mathbf{r}) \cdot (\mathbf{r} - \mathbf{r}')}{4\pi|\mathbf{r} - \mathbf{r}'|^3} d\Gamma(\mathbf{r}') - \frac{2}{D} \sum_j r_j(C(\mathbf{r}_j)) \frac{n(\mathbf{r}) \cdot (\mathbf{r}_j - \mathbf{r})}{4\pi|\mathbf{r}_j - \mathbf{r}|^3} \tag{7}$$

Equations (6) and (7) compose a set of algebraic equations for $\{C(\mathbf{r}_j)\}$ coupled to an integral equation for $\sigma(\mathbf{r})$. For the simulations described below, the surface integrals were solved numerically by discretizing the continuous surface into 400 boundary elements (20 in the θ-direction × 20 in the z-direction), each with constant density σ_k (k = 1–40), which approximates the integral equation as a set of coupled algebraic equations for $\{C(\mathbf{r}_j)\}$ and $\{\sigma_k\}$. Integrals over boundary elements were calculated numerically by Gauss-Legendre quadrature (order 10).

D. Filament Mechanics

A principal goal of the simulation approach is to account for filament orientation effects and filament interactions with the surface while at the same time avoiding the complications of simulating filament–filament interactions within the network. Similar to previous models by Mogilner and Oster[29] and Dickinson and Purich,[12] the approach is to treat only a segment of length L near the microbial surface and assume the rest of the filament length at further distances into the tail is immobilized in position and orientation. (Potential ways to relax this assumption are mentioned in the "Discussion" section.)

The force vector $\mathbf{F}_i$ exerted by filament i on the microbial surface is related to the displacement of the NPF position ($\mathbf{r}_i$) relative to the equilibrium position of the filament end at $\mathbf{r}_{0,i} + \mathbf{n}_i L$, where $\mathbf{r}_{0,i}$ and $\mathbf{n}_i$ are the position and tangent vector, respectively, at the position where the filament is assumed anchored into the actin network. The net displacement is assumed to be the sum of a filament tip displacement and a displacement due to stretching of the motor. Linear (spring-like) force–displacement relationships are assumed for the lateral and longitudinal filament tip displacements (with stiffnesses $\kappa_{f,\perp} = 3\lambda k_B T/L^3$ and $\kappa_{f,||} = k_B T \lambda^2/L^4$, respectively[21,25]) and motor stretching (with stiffness κ_m), such that the force-displacement relationship is

$$\mathbf{F}_i = -\mathbf{K}_i \{ \mathbf{r}_i - (\mathbf{r}_{0,i} + \mathbf{n}_i L) \} \tag{8}$$

where the stiffness tensor $\mathbf{K}_i$ is given by

$$\mathbf{K}_i = \left(\frac{1}{\kappa_{f,||}} + \frac{1}{\kappa_m} \right)^{-1} \mathbf{n}_i \mathbf{n}_i + \left(\frac{1}{\kappa_{f,\perp}} + \frac{1}{\kappa_m} \right)^{-1} (1 - \mathbf{n}_i \mathbf{n}_i) \tag{9}$$

The linear force–displacement assumption neglects filament buckling, which is expected only at much larger compressive forces ($\gtrsim$35 pN) than can be achieved by elongation.

When a filament adds a monomer to extend its length by d, a constant segment length L is maintained in the simulations by incrementally adjusting the position of $\mathbf{r}_{0,i}$ on the filament arc by the distance

$$\delta \mathbf{r}_{0,i} = \mathbf{n}_i d \tag{10}$$

The tangent vector of the filament at the anchor position is also adjusted by

$$\delta \mathbf{n}_i = \frac{\mathbf{n}_i \times (\mathbf{n}_i \times \mathbf{F}_i) d}{\kappa_{\mathrm{f},\perp} L^2} (1 - d/2L) \tag{11}$$

to account for the filament bending at the anchored end. In this way, $\mathbf{n}_i$ slowly reorients in response to a flexural force as the filament grows.

Finally, if the NPF is not rotationally compliant on the bacterial surface, processive elongation is expected to generate torsion on the actin filament and thus an additional torque on the microbial surface. The magnitude of filament torque τ, if it exists, is not known, but it likely depends on properties of the NPF-filament interaction and rotational friction of the NPF on the surface and between the filament and the NPF. To explore the effect of filament torque while avoiding specifying these known properties, a constant value of τ was assigned in some simulations.

Finally, to account for steric repulsion between the bacterial surface and the filament network, a strong repulsive force on the microbial surface was assumed to be generated when the surface boundary crosses an anchor position, $\mathrm{r}_{0,i}$. This force is assumed to be linear with position and directed normal to the surface such that it can be written

$$\mathbf{F}_{\mathrm{s},i} = \begin{cases} \kappa_{\mathrm{s}} \Delta \mathbf{r}_i \left(1 - R \|\Delta \mathbf{r}_i\|^{-1}\right) & \text{for } \|\Delta \mathbf{r}_i\| < R \\ 0 & \text{for } \|\Delta \mathbf{r}_i\| \geq R \end{cases} \tag{12}$$

where $\Delta \mathbf{r}_i$ is vector directed normal to the surface, given by

$$\Delta \mathbf{r}_i = \begin{cases} \mathbf{r}_{o.i} - \mathbf{r}_{\mathrm{p}} & \text{for } \mathbf{k}_3 \cdot \left(\mathbf{r}_{o.i} - \mathbf{r}_{\mathrm{p}}\right) < 0 \\ \left(1 - \mathbf{k}_3 \mathbf{k}_3\right)\left(\mathbf{r}_{o.i} - \mathbf{r}_{\mathrm{p}}\right) & \text{for } 0 \leq \mathbf{k}_3 \cdot \left(\mathbf{r}_{o.i} - \mathbf{r}_{\mathrm{p}}\right) < L_{\mathrm{s}} \\ \left(\mathbf{r}_{o.i} - \left(\mathbf{r}_{\mathrm{p}} + \mathbf{k}_3 L_{\mathrm{s}}\right)\right) & \text{for } \mathbf{k}_3 \cdot \left(\mathbf{r}_{o.i} - \mathbf{r}_{\mathrm{p}}\right) \geq L_{\mathrm{s}} \end{cases} \tag{13}$$

Considering both polymerization and steric forces, the net force and torque are:

$$\mathbf{F} = \sum_{j=1}^{N} \mathbf{F}_i + \mathbf{F}_{\mathrm{s},i} \tag{14}$$

and

$$\mathbf{T} = \sum_{i=1}^{N} \mathbf{r}_i \times \mathbf{F}_i + \mathbf{r}_{o,i} \times \mathbf{F}_{\mathrm{s},i}, \tag{15}$$

respectively.

E. Filament Nucleation and Detachment

Filaments under tension are assumed to detach with an exponentially increasing probability per unit time (i.e., the Bell model for protein bond rupture[3]):

$$k_{\mathrm{d}} = k_{\mathrm{d},0} \exp\left(\frac{|\mathbf{F}_i|}{F_{\mathrm{c}}}\right) \tag{16}$$

Vacated NPF's can then nucleate new filaments with probability per unit time k_{n}. New filaments initially grow from the NPF with random orientation that is uniformly distributed on the half-sphere relative to the outward normal vector at the surface. After reaching a length L, these nascent filaments then bind to a new network position $\mathbf{r}_{0i}$ and begin exerting force.

F. Parameter Estimates

This model requires several input parameters (summarized in Table 1), most of which can be calculated or estimated from the literature. The sensitivity of the model predictions over a reasonable range of values is also indicated in Table 1. Importantly, the key qualitative predictions (i.e., filament alignment in the direction of motion and rotational/helical trajectories) are not highly sensitive to the precise parameter values over their reasonable ranges, except where otherwise noted.

The length L of filament segment spanning the surface and the highly cross-linked actin network was set to 100 nm, in the range 50–200 nm that is typically assumed.[30] Assuming NPF's elongate processively similar to formins, which can operate on a (+)-end for well over 100 s,[23] we take $k_{\mathrm{d},0}$ to be small (~0.01 s). The filament detachment force on vesicles where ActA was linked to the phospholipid vesicle via histidine–nickel bond was estimated by Upadhyaya *et al.*[46] to be ~5–10 pN. It is likely NPF's and/or filaments are anchored more tightly to the native bacterial surfaces, hence we assume an upper value of $F_{\mathrm{c}} = 10$ pN in this range. Noting typical protein stiffness are ~1–10 pN/nm[20] but also recognizing the likely compliance of the bacterial cell wall, a lower value in the range ($\kappa_{\mathrm{m}} = 1$ pN/nm) was used. The value of filament torque τ was set to zero except where the sensitivity on this parameter was explored as noted below. Assuming an upper limit of ~14 $k_{\mathrm{B}}T$ on the available energy per monomer,[11] a reasonable upper bound on τ is then 30 $k_{\mathrm{B}}T$, based on the work at constant torque required to add monomer and thereby increase filament torsion by the amount $13/2\pi$ (determined by the filament pitch of 13 subunits). The on-rate constant k_{on} of monomers to plus-end is 10 $\mu\mathrm{M}^{-1}\mathrm{s}^{-1}$,[34] and this value was used for monomer binding to end-tracked filaments (although some evidence suggests faster binding to end-tracking motors[37]), and $k_{\mathrm{t},0}$ was assigned a value of 10^4 s^{-1}, which allows force-insensitive polymerization in Eq. (3) up to a few pN, as suggested by some experiments.[13] The nucleation rate k_{n} is expected to be highly variable depending on solutions conditions and NPF's. Its value has the primary effect of governing

the fraction of NPF's with anchored filaments, but its value otherwise does not strongly effect the key qualitative predictions. Nucleation and appearance of filaments on the bacterial surface and on biomimetic particles usually occurs in a matter of seconds, so $k_n = 1\ s^{-1}$ was used to reflect this time scale. The bulk monomer concentration C_∞ was set to 4 μM, within the range of profilin–actin concentration for extract experiments.[26] The NPF density was set to $10^3\ \mu m^{-2}$, corresponding to ~30-nm filament spacing.[1,40] Close estimation of drag coefficients β and β_r is unnecessary for the simulation because over a wide range of values filament forces rapidly approach a quasi-equilibrium between monomer-addition steps. Nevertheless, their values were approximated as 0.07 pN s/μm and 0.05 pN μm s, respectively, which correspond to the translational and rotational drag on a sphere of radius R in a medium with viscosity ten times greater than water, reflecting a more-viscous media in motility experiments. The diffusion coefficient of 5 $\mu m^2/s$ has been estimated for diffusion in actin tails[32,33] and for the cytoplasm.[27] The model is only weakly sensitive to the steric repulsion surface stiffness, κ_s, for $\kappa_s >> \kappa_m$. A value of $\kappa_s = 10$ pN/nm was assumed.

G. Simulation Method

Equations (1) and (2) were integrated by the implicit Euler method with time increment $\delta t = 2$ ms. Because the mechanical forces remain in quasi-equilibrium on the relevant (long) time-scale, such a long time step was suitable for these simulations, and the implicit Euler method essentially provides the solution to the mechanical equilibrium at each time step following monomer addition and filament detachment events. Filaments were initially oriented normal to the microbial surface. To speed the simulation, the slowly evolving monomer concentration field was updated only once every twenty time steps. Also because the local monomer concentration field $C(\mathbf{r})$ varied slowly during the simulation, the monomer concentration from the previous time step could be used in the denominator of Eq. (3) (which linearizes the algebraic system arising from Eqs. 6 to 7) with negligible loss of accuracy. Individual filaments were allowed to grow stochastically with probability for a monomer addition to a filament tip within each time increment δt equal to $r(F)\delta t$.

RESULTS

Figure 4 shows the predicted monomer concentration fields surrounding the bacterium as calculated by the solution to Eqs. (6) and (7) for the distribution of NPF-bound filament tips shown. Each elongating filament tip acts as a consumption point for monomers at the bacterial surface thereby contributing to the local depletion of monomers. As expected, the concentration field agrees closely (insert) with the distribution arising from corresponding continuous surface density $\rho(\mathbf{r})$ of filament tips, with small deviations attributed to spatial fluctuations in the discrete filament distribution relative to the continuous density. An important prediction is that monomer consumption creates monomer concentration gradient along the bacterial surface thereby causing a spatial variation in elongation rates and ultimately a differential in filament stresses.

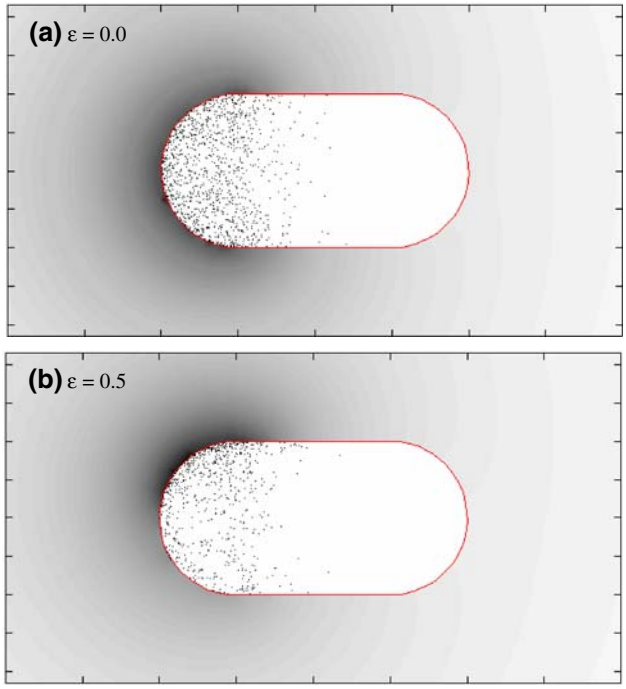

FIGURE 4. Predicted monomer concentration profile around the model bacterium. The key parameters for these calculations are radius $R = 0.4\ \mu m$, diffusivity $D = 5\ \mu m^2/s$, and maximum filament tip density, $\rho_0 = 10^3\ \mu m^{-2}$. Profiles are shown for two values of the wrapped Cauchy distribution dispersion parameter, $\varepsilon = 0.0$ (a) and $\varepsilon = 0.5$ (b). The points indicate positions of NPF-bound filament tips, which serve as points of monomer consumption.

Simulated bacterial trajectories are shown in Fig. 5 for symmetric and asymmetric NPF densities. In each case, after an initial lag period of symmetry-breaking, a steady trajectory emerges as filaments are pulled nearly into a new distribution predominantly aligned with the bacterial axis, thereby approaching a constant speed, torsion rate and mean filament orientation (Fig. 6), reflecting the emergent pattern of filament orientations and forces (Figs. 7 and 8, respectively). In the simulations, filaments initially work in competition with

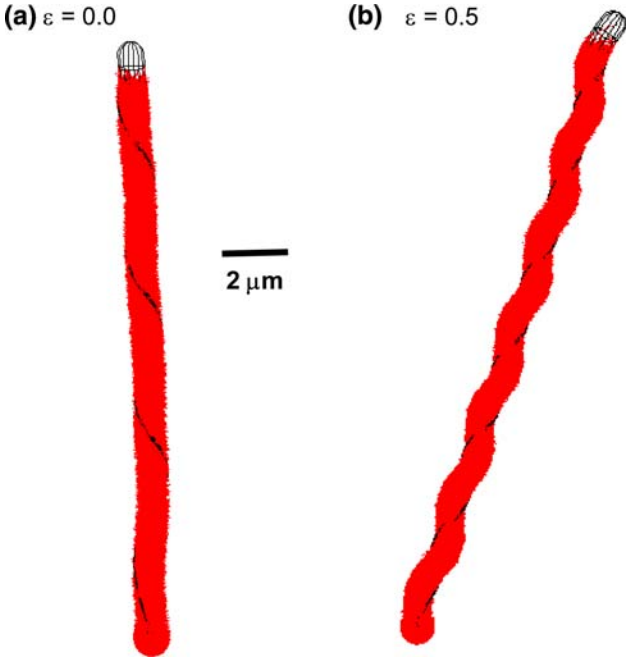

FIGURE 5. Simulated trajectories of the model bacteria, corresponding to the distributions in Fig. 4. (a) Axi-symmetric distribution. (b) Asymmetric distribution (Cauchy distribution parameter $\varepsilon = 0.5$), exhibiting helicity. Red points represent snapshots of filament anchor positions $\{r_{0,i}\}$ taken at 1-s intervals over the ~450-s simulation.

each other without yielding forward motion, but eventually symmetry is broken and filaments become pulled nearly into alignment with the axis of motion, allowing a steady-state speed, curvature, and torsion are reached. Speed and tail curvature reach a steady state rapidly, but the torsion takes a few minutes of simulation time before a steady state emerges.

Interestingly, simulated paths consistently evolved to a constant torsion, either right or left-handed with equal probability, when the individual filament torque τ was set to zero. The emergence of a steady torsion in the absence of torque can be explained considering that torsion allows the outermost filaments, whose tips exist in higher monomer concentrations, to take longer paths and thus accommodate their faster growth rate and thereby minimize the stress differential between faster and slower filaments. When NPF's are distributed asymmetrically around the bacterial axis, a helical trajectory arises (Fig. 5b), with steady-state curvature that is generated by the azimuthal variance in filament elongation rates.

The emergence of a steady torsion in the absence of a torque from individual filaments suggest that steady longitudinal rotation of *Listeria* reported by Robbins and Theriot[36] and the helical trajectories of *Listeria* reported by Zeile *et al.*[47] may have arisen from diffusion-limited elongation of end-tracked filaments, without requiring the filament torque expected to result from insertational elongation of helical filaments attached to non-rotationally compliant surface NPF's. However, a right-handed filament torque may bias the initial breakage of symmetry toward right-handed rotation, thereby contributing to the observation of only right-handed helices by Zeile *et al.* To address this possibility, simulations were performed to measure the frequency of right- or left-handed rotations as at various values of filament torque. Since the model and simulation are otherwise symmetric (beyond the initial NPF placement), an emergent torsion in either direction was equally probable, but generation of a right-handed torsion was consistently found for small values of torque of $\sim k_B T$. Therefore, these simulations support an alternative interpretation for the helical *Listeria* trajectories: torsion may arise from diffusion limitations alone, but the breakage in symmetry toward right-handed torsion might arise from filament torque. In any case, these simulations support with the general interpretation offered by Zeile *et al.*, i.e., that the right-handed helical paths are a consequence of elongation of right-handed helical filaments anchored at their (+)-ends to the bacterial surface.

The propulsion of biomimetic particles coated with NPF's often exhibit less persistent curvature and torsion than shown by *Listeria*.[41] Also, some EM micrographs of tails behind particles show a more random orientation of filaments in the comet tail.[6] A potential explanation for this difference is that surface-adsorbed NPF's provide poor anchorage for end-tracked filaments, and frequent filament detachment and rapid turnover of the ensemble of attached filaments precludes network alignment as well as persistent curvature and torsion. To explore this possibility, simulations were performed with a lower value of the characteristic detachment force, F_c. As shown in Fig. 9, the smaller attachment strength yields trajectories that are much different from the persistent trajectories in Fig. 5. These trajectories were characterized by much higher curvature and frequent changes in torsion direction, similar to the behavior recently reported for biomimetic particles.[41] In addition, the filaments did not become predominantly aligned with the direction of motion, because most filaments detached by force soon after integrating into the actin tail before they could align. For this type of motion, the persistence could be further reduced by increasing the segment length, L, as shown in Fig. 9d. These predictions suggest that the strength of NPF and/or filament (+)-end attachment may govern the persistence in trajectories. Unlike the native situation, the physi-adsorbed NPF's coating biomimetic particles are presumably less tightly bound and not optimally presented to end-track filaments.

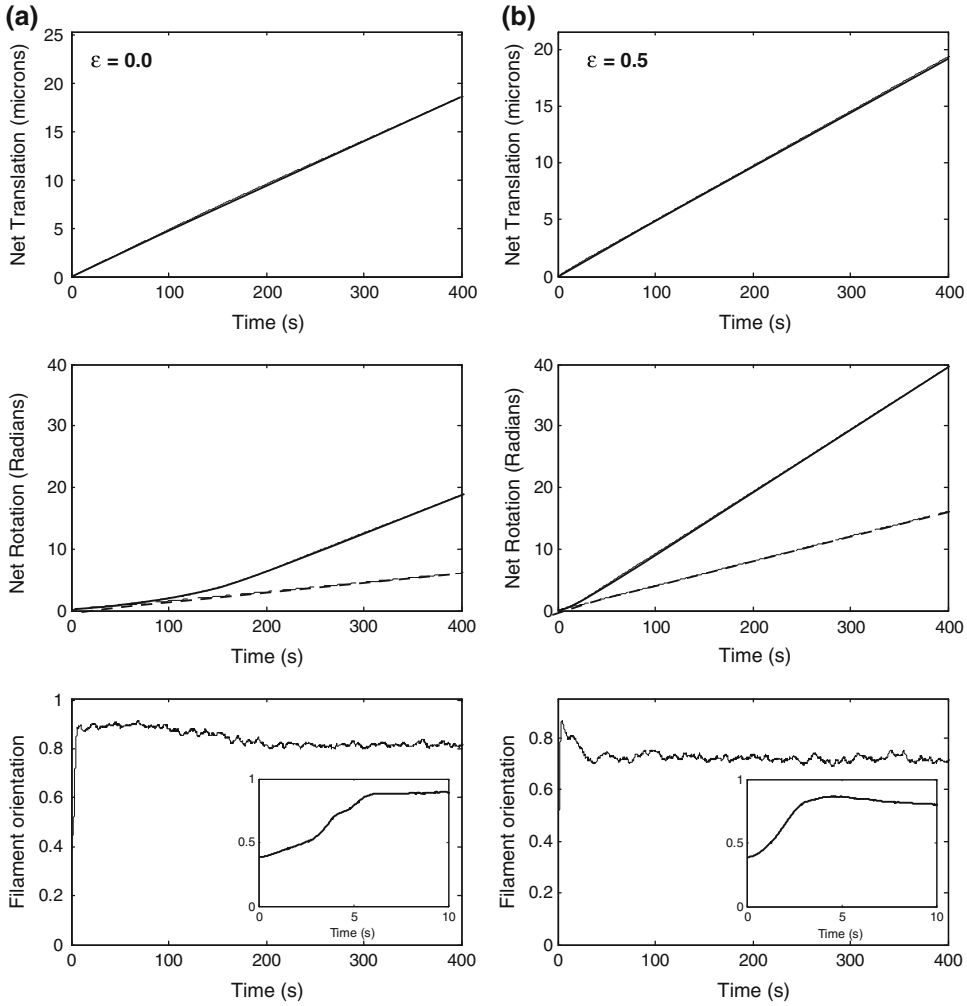

FIGURE 6. Time profiles of (a) the net translation, (b) the net rotations (solid line = torsion; dashed line = pitch), and (c) the mean filament orientation in the propulsion direction (<$n_f k_3$>) for the trajectory from Fig. 5a. As indicated by the slopes of these curves, the speed and curvature of the trajectory reach a steady state quickly, whereas torsion takes several minutes of simulation time to ultimately reach a steady state. (d–e) show the corresponding plots from the trajectory in Fig. 5b.

DISCUSSION

The predictions and simulation results of this mechanistic model suggest that some puzzling properties of actin-based bacterial propulsion, such as alignment of working filaments with the direction of propulsion, rotation about the longitudinal axis, and helical trajectories, should arise naturally from diffusion-limited, processive elongation of filaments that are persistently attached at their elongating (+)-ends. A steady-state trajectory, exhibiting persistent speed, torsion, and curvature, emerges as filaments become slowly pulled into a steady-state distribution of orientations for a given fixed surface distribution of nucleation promoting factors (e.g., ActA).

The simulation method proposed here differs from previously proposed models and simulations for actin-based propulsion of *Listeria* in several respects. First, unlike previous continuum models for propulsion (e.g., Gerbal *et al.*,[15] Rutenberg and Grant[38]), the multi-scale simulation proposed here accounts for individual filament orientations and their forces on the bacterial surface, and allows an accounting for the effect of filament re-orientation on the trajectories. Second, unlike our previous one-dimensional filament-scale simulation[12] and those of others,[16,28] this three-dimensional simulation accounts for the three-dimensional filament re-orientation and stresses, thereby allowing new patterns that could emerge in a one-dimensional simulation. This model also differs from the three-dimensional filament-scale simulations of Alberts and Odell,[2] which did not account for elastic deformation and reorientation of filament tips and assumed forward displacements was achieved by rectified Brownian motion of the bacterium upon filament

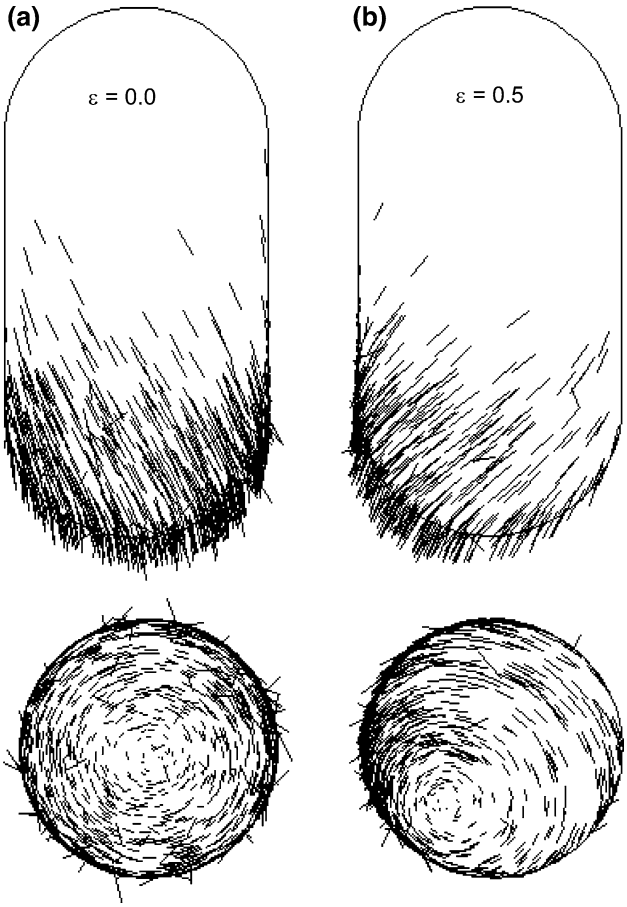

FIGURE 7. Filament distribution after the emergence of a steady filament orientation pattern for the axisymmetric NPF distribution and asymmetric NPF distribution, corresponding to the trajectories from Figs. 5a (a) and 5b (b), respectively. Side and bottom views are shown.

detachment. The simulations presented here did not account for Brownian fluctuations, which were expected to be insignificant under the tight force balance between pushing and pulling filaments. This assumption is consistent with high-resolution tracking results of Kuo and McGrath,[24] who estimated that thermal fluctuations of propelled *Listeria* to be extremely small (less than 0.1 nm). Finally, as in our previous one-dimensional model,[12] but contrary to most other published models, we assume working filaments elongate while persistently attached to the bacterial surface by filament end-tracking motors. Most importantly, the results of the simulations show that the filament end-tracking mechanism yields aligned filament distributions and rotating or helical trajectories with persistent curvature and torsion. These experimentally reported properties have not been previously explained by a mechanistic model.

In the simulations presented here, the presence of Arp2/3-mediated branches, which can be abundant

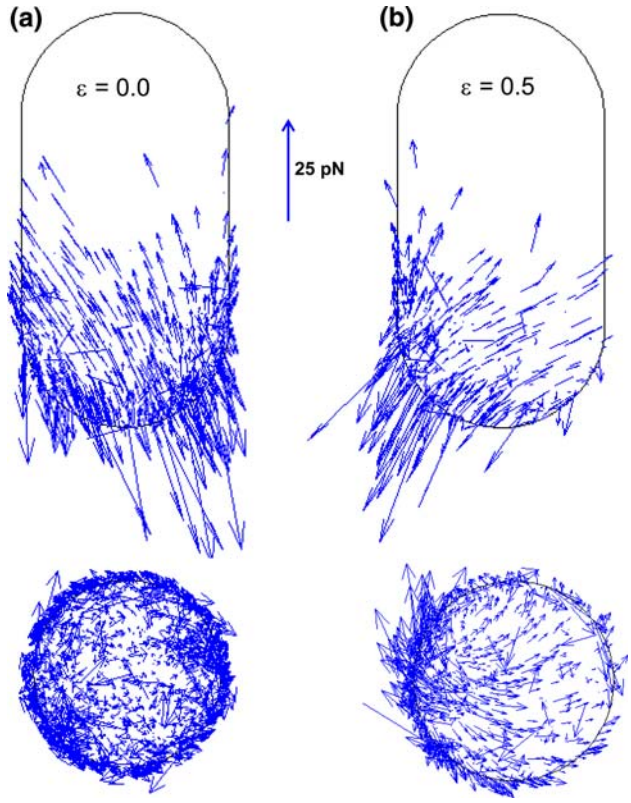

FIGURE 8. Filament force vectors after the emergence of a steady filament orientation pattern, corresponding to Fig. 7 and the trajectories from Figs. 5a (a) and 5b (b). Side and bottom views are shown.

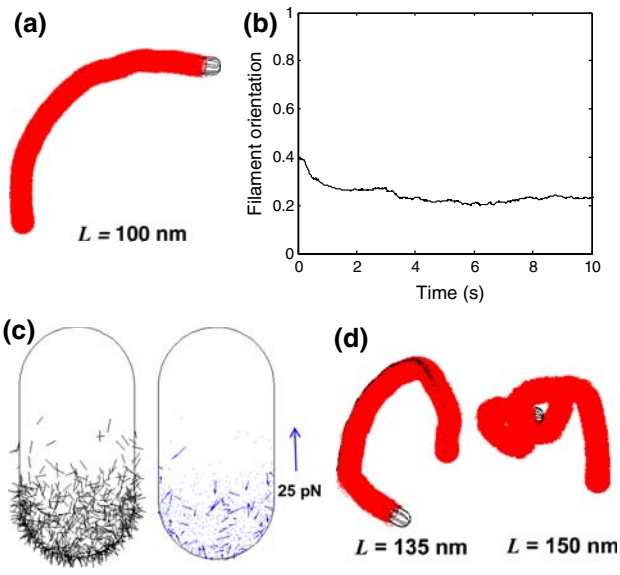

FIGURE 9. Simulated trajectory with reduced characteristic bond strength, F_c = 1 pN (L = 100 nm, exhibiting much less persistence in torsion and curvature that for F_c = 10 pN, and presenting a more random filament orientation (compare to Fig. 5). (a) Trajectory. (b) Mean filament orientation ($\langle n_f k_3 \rangle$) vs. time. (c) Force vectors and filament distribution. (d) Trajectories for two larger values filament segment lengths shown.

during *Listeria* motility under some conditions (Fig. 1), was ignored, but it is recognized that the tips of these branches should also consume monomers (until capped by capping protein) thus contribute to the local depletion in monomer concentration. Consistent with this assumption and the "funneling" hypothesis,[7] several studies have shown that capping filament branches enhances propulsion speed.[39] However, the funneling hypothesis alone does not explain how "mother" filaments associated with the surface remain uncapped and become aligned parallel with the direction of propulsion. Simulation of the additional monomer consumption by filament branches (until capped) can easily be treated with a straight-forward modification of the present model.

While the simulations support new explanations for some previously unexplained properties of actin-based propulsion, this model has a number of limitations that will be improved in future refinements. First, all elastic properties of the actin network near the surface are captured by the free segment length L, thereby avoiding a detailed treatment of filament–filament interactions. It is possible that explicit accounting for filament–filament interactions in the zone near the surface could significantly affect the surface stresses or the filament alignment process in an unforeseen way. Also, in the simulations the F-actin network outside this zone was assumed rigid, such that all actin elastic stresses are stored entirely in the flexure filament segments near the surface. This assumption, which neglects the possible elastic deformation in the cross-linked actin network, is most unrealistic at the bacterial sides where the F-actin cup surrounding the bacterium is thin. The simulations predict a pitch of a few microns rather than those of 10s of microns reported experimentally. It is possible that dissipation of stress in the tail limits the torsion thereby yielding longer pitches than those predicted in the simulations. A more realistic simulation approach would allow filament forces to generate tail deformations and displacements of the anchor positions $\{\mathbf{r}_{0,i}\}$. One approach would be to treat such deformations by coupling the filament scale simulations to a continuum model for the actin tail. Despite these limitations, the simulations do capture the essence of the phenomena and provide reasonable explanations of filament reorientation as well as the mechanism for rotational and helical trajectories.

ACKNOWLEDGMENT

This work was supported by a grant from the National Science Foundation (CTS-0505929).

REFERENCES

[1]Abraham, V. C., V. Krishnamurthi, D. L. Taylor, and F. Lanni. The actin-based nanomachine at the leading edge of migrating cells. *Biophys. J.* 77:1721–1732, 1999.

[2]Alberts, J. B., and G. M. Odell. *In silico* reconstitution of Listeria propulsion exhibits nano-saltation. *PLoS Biol.* 2:e412, 2004.

[3]Bell, G. I. Models for the specific adhesion of cells to cells. *Science* 200:618–627, 1978.

[4]Brebbia, C. A. Boundary Element Techniques. New York: Springer-Verlag, 1984.

[5]Brieher, W. M., M. Coughlin, and T. J. Mitchison. Fascin-mediated propulsion of *Listeria monocytogenes* independent of frequent nucleation by the Arp2/3 complex. *J. Cell Biol.* 165:233–242, 2004.

[6]Cameron, L. A., T. M. Svitkina, D. Vignjevic, J. A. Theriot, and G. G. Borisy. Dendritic organization of actin comet tails. *Curr. Biol.* 11:130–135, 2001.

[7]Carlier, M. F., C. Le Clainche, S. Wiesner, and D. Pantaloni. Actin-based motility: from molecules to movement. *Bioessays* 25:336–345, 2003.

[8]Chereau, D., and R. Dominguez. Understanding the role of the G-actin-binding domain of Ena/VASP in actin assembly. *J. Struct. Biol.* 155:195–201, 2006.

[9]Chereau, D., F. Kerff, P. Graceffa, Z. Grabarek, K. Langsetmo, and R. Dominguez. Actin-bound structures of Wiskott-Aldrich syndrome protein (WASP)-homology domain 2, the implications for filament assembly. *Proc. Natl. Acad. Sci. USA* 102:16644–16649, 2005.

[10]Co, C., D. T. Wong, S. Gierke, V. Chang, and J. Taunton. Mechanism of actin network attachment to moving membranes: barbed end capture by N-WASP WH2 domains. *Cell* 128:901–913, 2007.

[11]Dickinson, R. B., L. Caro, and D.L. Purich. Force generation by cytoskeletal filament end-tracking proteins. *Biophys. J.* 87:2838–2854, 2004.

[12]Dickinson, R. B., and D. L. Purich. Clamped-filament elongation model for actin-based motors. *Biophys. J.* 82:605–617, 2002.

[13]Dickinson, R. B., and D. L. Purich. Diffusion rate limitations in actin-based propulsion of hard and deformable particles. *Biophys. J.* 91:1548–1563, 2006.

[14]Fisher, N. I. Statistical Analysis of Circular Data. Cambridge: Cambridge University Press, 1993.

[15]Gerbal, F., P. Chaikin, Y. Rabin, and J. Prost. An elastic analysis of *Listeria monocytogenes* propulsion. *Biophys. J.* 79:2259–2275, 2000.

[16]Gholami, A., M. Falke, and E. Frey. Velocity oscillations in actin-based motility. *New J. Phys.* 10:1–12, 2008.

[17]Gouin, E., C. Egile, P. Dehoux, V. Villiers, J. Adams, F. Gertler, R. Li, and P. Cossart. The RickA protein of *Rickettsia conorii* activates the Arp2/3 complex. *Nature* 427:457–461, 2004.

[18]Gouin, E., H. Gantelet, C. Egile, I. Lasa, H. Ohayon, V. Villiers, P. Gounon, P. J. Sansonetti, and P. Cossart. A comparative study of the actin-based motilities of the pathogenic bacteria *Listeria monocytogenes*, *Shigella flexneri* and *Rickettsia conorii*. *J. Cell Sci.* 112(Pt 11):1697–1708, 1999.

[19]Holmes, K. C., D. Popp, W. Gebhard, and W. Kabsch. Atomic model of the actin filament. *Nature* 347:44–49, 1990.

[20]Howard, J. Mechanics of Motor Proteins and the Cytoskeleton. Sunderland, MA: Sinauer, 2001.

[21]Isambert, H., and A. C. Maggs. Dynamics and rheology of actin solutions. *Macromolecules* 29:1036–1040, 1996.
[22]Isambert, H., P. Venier, A. C. Maggs, A. Fattoum, R. Kassab, D. Pantaloni, and M. F. Carlier. Flexibility of actin filaments derived from thermal fluctuations. Effect of bound nucleotide, phalloidin, and muscle regulatory proteins. *J. Biol. Chem.* 270:11437–11444, 1995.
[23]Kovar, D. R., and T. D. Pollard. Insertional assembly of actin filament barbed ends in association with formins produces piconewton forces. *Proc. Natl. Acad. Sci. USA* 101:14725–14730, 2004.
[24]Kuo, S. C., and J. L. McGrath. Steps and fluctuations of *Listeria monocytogenes* during actin-based motility. *Nature* 407:1026–1029, 2000.
[25]Landau, L. D., and E. M. Lifshitz. Theory of Elasticity. 3rd ed. Oxford: Pergamon Press, 1986.
[26]Marchand, J. B., P. Moreau, A. Paoletti, P. Cossart, M. F. Carlier, and D. Pantaloni. Actin-based movement of *Listeria monocytogenes*: actin assembly results from the local maintenance of uncapped filament barbed ends at the bacterium surface. *J. Cell Biol.* 130:331–343, 1995.
[27]McGrath, J. L., Y. Tardy, C. F. Dewey, Jr., J. J. Meister, and J. H. Hartwig. Simultaneous measurements of actin filament turnover, filament fraction, and monomer diffusion in endothelial cells. *Biophys. J.* 75:2070–2078, 1998.
[28]Mogilner, A., and L. Edelstein-Keshet. Regulation of actin dynamics in rapidly moving cells: a quantitative analysis. *Biophys. J.* 83:1237–1258, 2002.
[29]Mogilner, A., and G. Oster. Cell motility driven by actin polymerization. *Biophys. J.* 71:3030–3045, 1996.
[30]Mogilner, A., and G. Oster. Polymer motors: pushing out the front and pulling up the back. *Curr. Biol.* 13:R721–R733, 2003.
[31]Mogilner, A., and G. Oster. Force generation by actin polymerization II: the elastic ratchet and tethered filaments. *Biophys. J.* 84:1591–1605, 2003.
[32]Paluch, E., J. van der Gucht, J. F. Joanny, and C. Sykes. Deformations in actin comets from rocketing beads. *Biophys. J.* 91:3113–3122, 2006.
[33]Plastino, J., I. Lelidis, J. Prost, and C. Sykes. The effect of diffusion, depolymerization, nucleation promoting factors on actin gel growth. *Eur. Biophys. J.* 33:310–320, 2004.
[34]Pollard, T. D., L. Blanchoin, and R. D. Mullins. Molecular mechanisms controlling actin filament dynamics in nonmuscle cells. *Annu. Rev. Biophys. Biomol. Struct.* 29:545–576, 2000.
[35]Rafelski, S. M., and J. A. Theriot. Bacterial shape and ActA distribution affect initiation of *Listeria monocytogenes* actin-based motility. *Biophys. J.* 89:2146–2158, 2005.
[36]Robbins, J. R., and J. A. Theriot. *Listeria monocytogenes* rotates around its long axis during actin-based motility. *Curr. Biol.* 13:R754–R756, 2003.
[37]Romero, S., C. Le Clainche, D. Didry, C. Egile D. Pantaloni, and M. F. Carlier. Formin is a processive motor that requires profilin to accelerate actin assembly and associated ATP hydrolysis. *Cell* 119:419–429, 2004.
[38]Rutenberg, A. D., and M. Grant. Curved tails in polymerization-based bacterial motility. *Phys. Rev. E Stat. Nonlin. Soft Matter Phys.* 64:021904, 2001.
[39]Samarin, S., S. Romero, C. Kocks, D. Didry, D. Pantaloni, and M. F. Carlier. How VASP enhances actin-based motility. *J. Cell Biol.* 163:131–142, 2003.
[40]Sechi, A. S., J. Wehland, and J. V. Small. The isolated comet tail pseudopodium of *Listeria monocytogenes*: a tail of two actin filament populations, long and axial and short and random. *J. Cell Biol.* 137:155–167, 1997.
[41]Shaevitz, J. W., and D. A. Fletcher. Curvature and torsion in growing actin networks. *Phys. Biol.* 5:26006, 2008.
[42]Stevens, J. M., E. E. Galyov, and M. P. Stevens. Actin-dependent movement of bacterial pathogens. *Nat. Rev. Microbiol.* 4:91–101, 2006.
[43]Stevens, M. P., J. M. Stevens, R. L. Jeng, L. A. Taylor, M. W. Wood, P. Hawes, P. Monaghan, M. D. Welch, and E. E. Galyov. Identification of a bacterial factor required for actin-based motility of *Burkholderia pseudomallei*. *Mol. Microbiol.* 56:40–53, 2005.
[44]Suzuki, T., H. Mimuro, S. Suetsugu, H. Miki, T. Takenawa, and C. Sasakawa. Neural Wiskott-Aldrich syndrome protein (N-WASP) is the specific ligand for Shigella VirG among the WASP family and determines the host cell type allowing actin-based spreading. *Cell Microbiol.* 4:223–233, 2002.
[45]Tsuchida, M. A., and J. A. Theriot. Decoupling the coupling: surface attachment in actin-based motility. *ACS Chem. Biol.* 2:221–224, 2007.
[46]Upadhyaya, A., J. R. Chabot, A. Andreeva, A. Samadani, and A. van Oudenaarden. Probing polymerization forces by using actin-propelled lipid vesicles. *Proc. Natl. Acad. Sci. USA* 100:4521–4526, 2003.
[47]Zeile, W. L., F. Zhang, R. B. Dickinson, and D. L. Purich. Listeria's right-handed helical rocket-tail trajectories: mechanistic implications for force generation in actin-based motility. *Cell Motil. Cytoskeleton* 60:121–128, 2005.